nature materials

Article https://doi.org/10.1038/s41563-024-01986-x

Cation-eutaxy-enabled III–V-derived van der Waals crystals as memristive semiconductors

Received: 14 June 2021

Accepted: 31 July 2024

Published online: 28 August 2024

A list of authors and their affiliations appears at the end of the paper

Novel two-dimensional semiconductor crystals can exhibit diverse physical properties beyond their inherent semiconducting attributes, making their pursuit paramount. Memristive properties, as exemplars of these attributes, are predominantly manifested in wide-bandgap materials. However, simultaneously harnessing semiconductor properties alongside memristive characteristics to produce memtransistors is challenging. Herein we prepared a class of semiconducting III–V-derived van der Waals crystals, specifically the $H_xA_{1-x}BX$ form, exhibiting memristive characteristics. To identify candidates for the material synthesis, we conducted a systematic high-throughput screening, leading us to 44 prospective III–V candidates; of these, we successfully synthesized ten, including nitrides, phosphides, arsenides and antimonides. These materials exhibited intriguing characteristics such as electrochemical polarization and memristive phenomena while retaining their semiconductive attributes. We demonstrated the gate-tunable synaptic and logic functions within single-gate memtransistors, capitalizing on the synergistic interplay between the semiconducting and memristive properties of our two-dimensional crystals. Our approach guides the discovery of van der Waals materials with unique properties from unconventional crystal symmetries.

Semiconducting two-dimensional (2D) materials based on group III–V compounds are tremendously promising for advancements in electronic and optoelectronic applications. However, exploring this class of 2D materials has encountered formidable challenges. While the widely used topochemical approach has successfully synthesized various 2D materials[1,2], semiconducting 2D materials with memristive capabilities have been more elusive. Memtransistors, characterized as three-terminal gate-tunable memristors, represent hybrid memristor–transistor structures that combine the memory properties of memristors with the switching capabilities of transistors. These structures harness the intrinsic weak electrostatic screening characteristics of low-dimensional materials and offer possibilities for simplifying addressability in crossbar arrays, as well as for enabling bio-realistic functionalities[3–6]. The primary challenge here lies in expanding the library of semiconducting van der Waals (vdW) materials, particularly those exhibiting memristive behaviours, through innovative soft chemistry methodologies[7]. In particular, soft chemistry methodologies including the selective removal of cation A from A–B–X ternary compounds to produce layered B–X compounds (where A and B represent cations and X an anion) have been pivotal for this purpose. While these chemistry techniques have produced various 2D transition metal oxides[8], sulfides[9] and MXenes[10], the synthesis of semiconducting 2D B–X compounds remains a rare achievement. Specifically, for III–V compounds known for their robust covalent bonds and distinctive structural preferences, such as zinc blende ($F\bar{4}3m$) or wurtzite ($P6_3mc$) structures, synthesizing freestanding III–V vdW crystals, particularly those with memristive properties, poses a substantial scientific challenge.

With this background, herein we prepared a class of semiconducting III–V-derived vdW crystals, specifically the $H_xA_{1-x}BX$ form, through topochemical etching; the crystals produced could be used as memtransistors. To obtain vdW crystals from ternary compounds via topochemical etching, we initiated our study by identifying ternary spaces with cation-eutaxy structures, as illustrated

e-mail: aloysius.soon@yonsei.ac.kr; jcheon@yonsei.ac.kr; cmpark@yonsei.ac.kr; jykim@kicet.re.kr; wshim@yonsei.ac.kr

https://doi.org/10.1038/s41563-024-01986-x

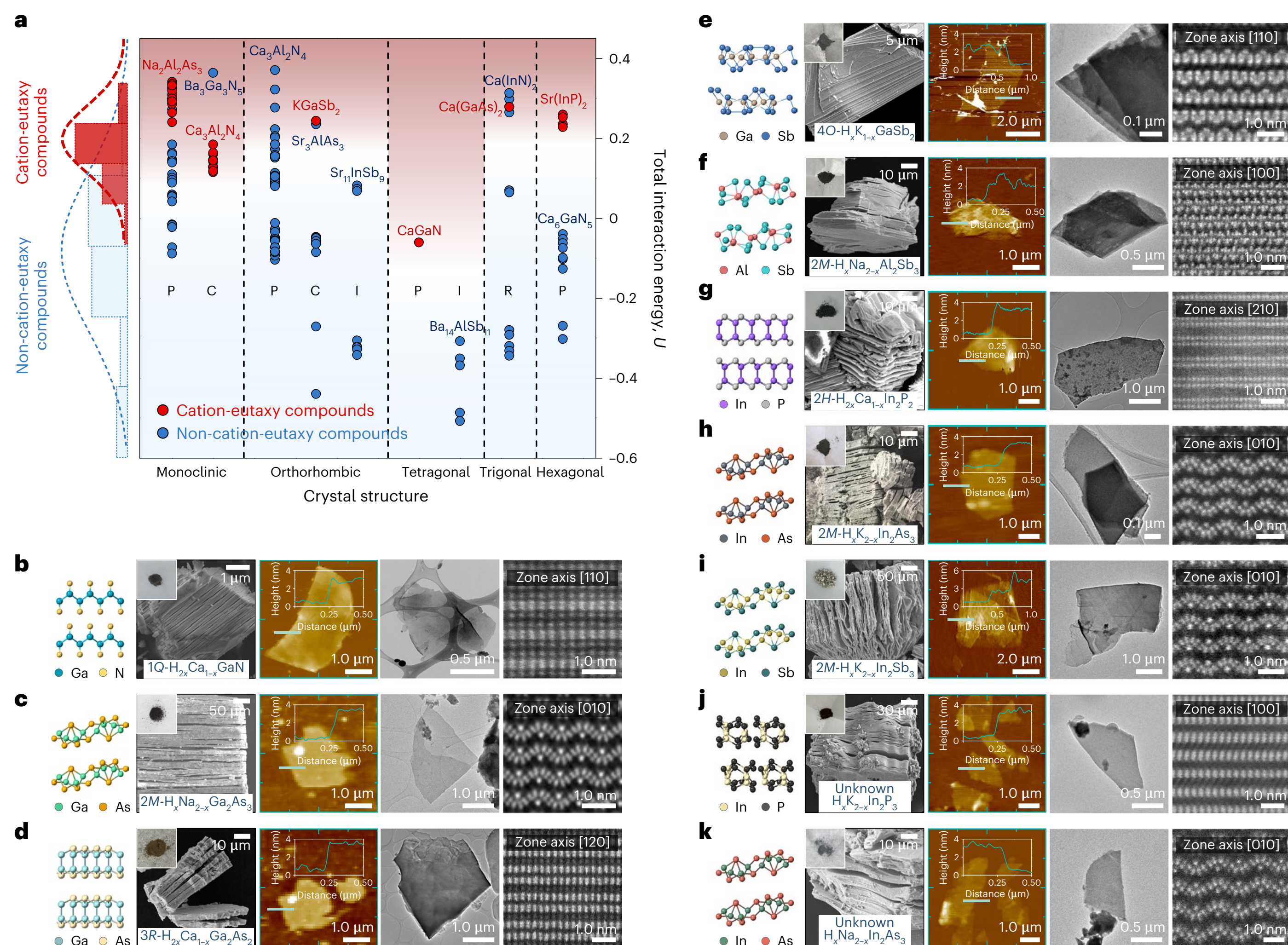

Fig. 1 | Experimental realization of the newly predicted protonated III–V vdW crystal. a, Quantitative physical model from Pauling's fourth rule[33]. We considered A–B repulsion, B–X attraction and A–X attraction in defining the total interaction energy U, which is required to form cation eutaxy. A higher A–B repulsion and higher B–X attraction can lead to cation eutaxy, which is indicated in the map differentiating the formation of cation-eutaxy ternary compounds (red area) from non-cation-eutaxy compounds (blue area). The symbols P, R, C and I represent primitive, rhombohedral, centered and inner Bravais lattices, respectively. **b**–**k**, Protonated III–V crystals reported herein are the layered structures of *1Q*-$H_{2x}Ca_{1-x}GaN$ (Ca, 6.0 at.%; **b**), *2M*-$H_xNa_{2-x}Ga_2As_3$ (Na, 2.1 at.%; **c**), *3R*-$H_{2x}Ca_{1-x}Ga_2As_2$ (Ca, 4.4 at.%; **d**), *4O*-$H_xK_{1-x}GaSb_2$ (K, 5.7 at.%; **e**), *2M*-$H_xNa_{2-x}Al_2Sb_3$ (Na, 4.6 at.%; **f**), *2H*-$H_{2x}Ca_{1-x}In_2P_2$ (Ca, 2.0 at.%; **g**), *2M*-$H_xK_{2-x}In_2As_3$ (K, 3.5 at.%; **h**), *2M*-$H_xK_{2-x}In_2Sb_3$ (K, 3.4 at.%; **i**), unknown $H_xK_{2-x}In_2P_3$ (K, 4.9 at.%; **j**) and $H_xNa_{2-x}In_2As_3$ (Na, 4.8 at.%; **k**). From left to right, each panel contains a model of multiple unit cells (not to scale), a SEM image of layered films with a photograph of the etched powder (inset), an AFM image of isolated nanosheets with the height profile (inset), a high-resolution TEM image of isolated nanosheets and the cross-sectional HAADF-STEM image.

in Supplementary Fig. 1. Through a multistep search process, we established specific criteria for what is classified as a cation-eutaxy crystal structure (details in the Methods) and identified 322 known ternaries meeting these criteria from the Inorganic Crystal Structure Database (ICSD)[11] and Materials Project database[12] (Supplementary Table 1). Further employing the pymatgen algorithm[13], we extracted 94 common crystal structures, termed prototypes (Supplementary Table 2). Subsequently, high-throughput screening was used to examine 3,510 elemental combinations for the A–B–X system, with cation A from group I and II metals, cation B from *d*-block and group III and IV elements and anion X from group V and VI elements, revealing 760 known cation-eutaxy ternaries, including 35 III–V-based compounds (Supplementary Table 3). Using these known compounds, a data-driven statistical model[14] generated 1,827 suggested compounds as potentially unknown compounds (Supplementary Table 4). Of these, 575 suggested compounds (including 15 III–V ternaries) were chosen for further density functional theory (DFT) evaluations (Supplementary Table 5), leading to the identification of 127 'unknown' compounds (details in the Methods). Notably, among the 15 suggested III–V ternaries, nine compounds were within the desired energy range, serving as promising candidates for III–V vdW crystal synthesis (Supplementary Fig. 2). Finally, we selected ten III–V-based cation-eutaxy ternaries, including eight known one (out of 35 known) and two newly predicted ones (out of nine unknown; Supplementary Fig. 3). Thus, this study presents the successful implementation of III–V-derived vdW crystals using known and unknown ternary compounds, highlighting the potential of diverse cation-eutaxy ternaries for further vdW crystal synthesis.

Library of III–V-derived vdW crystals

We propose a phenomenological model with which to visualize the stabilities of III–V-based cation-eutaxy ternary families and support this with experimental syntheses of ten unexplored III–V spaces. We used valence as a parameter and considered three possible interactions: (1) A–B repulsion, (2) B–X attraction and (3) A–X attraction. The total interaction energy U required for cation eutaxy can be written

as $U = |(Z_A \times Z_B)/d_{AB}| + |(Z_B \times Z_X)/d_{BX}| - |(Z_A \times Z_X)/d_{AX}|$, where Z_A, Z_B and Z_X are the products of the valence (Z) and atomic percentages (at.%) of cations A and B and anion X, respectively, and d_{ij} is the bond distance between ions i and j (details in the Methods). Based on this model, a higher repulsion of A–B and a higher attraction of B–X can lead to cation eutaxy. Figure 1a shows a clear boundary between III–V-based cation-eutaxy ternary compounds (upper region) and 3D-bonded ternary compounds (lower region) in terms of the interaction energy U (Supplementary Table 6), which can also be confirmed with the ICSD for the ternary compounds listed in Fig. 1a. In contrast to III–V-based ternary compounds, the U model does not provide distinct boundaries for transition metal-based compounds, which may arise from the multivalent states of cation B in A–B–X ternary compounds (Supplementary Fig. 4 and Supplementary Table 7).

To test the validity of our high-throughput library and model, we used III–V-derived vdW crystals from not only known cation-eutaxy A_x–B_y–X_z ternary compounds but also unknown cation-eutaxy ternary compounds. First, with the eight known ternary compounds ($CaGaN$, $Na_2Ga_2As_3$, $CaGa_2As_2$, $KGaSb_2$, $Na_2Al_2Sb_3$, $CaIn_2P_2$, $K_2In_2As_3$ and $K_2In_2Sb_3$), we performed proton-exchange reactions using acids to remove cation A to attain levels of <6.0 at.% (Supplementary Fig. 5a–h) and obtained protonated III–V vdW crystals of 1Q-$H_{2x}Ca_{1-x}GaN$ (Ca, 6.0 at.%), 2M-$H_xNa_{2-x}Ga_2As_3$ (Na, 2.1 at.%), 3R-$H_{2x}Ca_{1-x}Ga_2As_2$ (Ca, 4.4 at.%), 4O-$H_xK_{1-x}GaSb_2$ (K, 5.7 at.%), 2M-$H_xNa_{2-x}Al_2Sb_3$ (Na, 4.6 at.%), 2H-$H_{2x}Ca_{1-x}In_2P_2$ (Ca, 2.0 at.%), 2M-$H_xK_{2-x}In_2As_3$ (K, 3.5 at.%) and 2M-$H_xK_{2-x}In_2Sb_3$ (K, 3.4 at.%), where the symbols Q, M, R, O and H indicate tetragonal, monoclinic, rhombohedral, orthorhombic and hexagonal systems, respectively (Supplementary Methods). We observed the laminar structures using scanning electron microscopy (SEM) and analysed the mechanically exfoliated nanosheets dispersed on various surfaces (for example, Si or a carbon grid) using atomic force microscopy (AFM) and high-resolution transmission electron microscopy (TEM; Fig. 1b–i, middle three columns, from left to right, respectively, for the three methods). The TEM grids were subsequently sectioned using a focused ion beam and imaged using high-angle annular dark-field scanning transmission electron microscopy (HAADF-STEM; Fig. 1b–i, righthand column). Within the fields of view (1 µm × 1 µm), the electron diffraction patterns unequivocally showed different Bravais lattices, that is, tetragonal P for $H_{2x}Ca_{1-x}GaN$, monoclinic P for $H_xNa_{2-x}Ga_2As_3$, trigonal R for $H_{2x}Ca_{1-x}Ga_2As_2$, orthorhombic C for $H_xK_{1-x}GaSb_2$, monoclinic P for $H_xNa_{2-x}Al_2Sb_3$, hexagonal P for $H_{2x}Ca_{1-x}In_2P_2$, monoclinic P for $H_xK_{2-x}In_2As_3$ and monoclinic P for $H_xK_{2-x}In_2Sb_3$, where the symbols P, R and C indicate primitive, rhombohedral and centered Bravais lattices, respectively (Supplementary Fig. 6a–h). The cross-sectional STEM images presented evidence of atomic ordering in the samples with interlayer spacings that are comparable to or larger than 3 Å (Supplementary Discussion 1)[15], which indicated the presence of vdW bonds between the layers.

In addition, based on the high-throughput screening results (Supplementary Fig. 1), we synthesized two unknown cation-eutaxy ternary compounds ($K_2In_2P_3$ and $Na_2In_2As_3$; Supplementary Fig. 7). From $K_2In_2P_3$ and $Na_2In_2As_3$, we obtained semiconducting protonated III–V vdW $H_xK_{2-x}In_2P_3$ (K, 4.9 at.%) and $H_xNa_{2-x}In_2As_3$ (Na, 4.8 at.%) crystals (Fig. 1j–k, Supplementary Fig. 5i–j and Supplementary Methods) using topochemical etching. Both resulting protonated III–V vdW crystals, $H_xK_{2-x}In_2P_3$ and $H_xNa_{2-x}In_2As_3$, also exhibited a Bravais lattice, monoclinic P, different from the known zinc-blende structures of InP and InAs (Supplementary Fig. 6i–j). Additionally, we investigated the electrical properties of seven III–V protonated vdW crystals, which indicated p-type semiconductor characteristics (Supplementary Table 8).

Cation migration in synthesized $H_xK_{1-x}GaSb_2$ crystals

Our next step is to explore the memristive properties of these III–V materials. To observe these characteristics, three critical conditions must be met, including (1) semiconducting properties within the vdW crystal, (2) an exfoliable 2D crystal structure conducive to electrostatic gating and (3) 'open structures' that facilitate unimpeded cation migration (Supplementary Discussion 2). Longer A–X bond lengths increase the vdW gap after cation A etching, which ensures wide ionic migration pathways, resulting in a reduced activation energy barrier and high diffusivity[16]. $KGaSb_2$, with its ample interlayer spacing, enables migration of typical cation A (Li–K)-based A_x–B_y–Sb_z ternary compounds (Fig. 2a and Supplementary Fig. 8). Thus, we selected $KGaSb_2$ (*Cmca* space group) as a representative example. To create vdW 4O-$H_xK_{1-x}GaSb_2$ (referred to as $H_xK_{1-x}GaSb_2$ for simplicity), we performed K^+ ion substitution with the H^+ ion via a soft chemistry approach. Annular bright-field STEM images confirmed K^+ ion removal and preservation of the [$GaSb_2$] layered framework with its orthorhombic structure (Fig. 2b–c and Supplementary Fig. 9). Additional crystal structure and chemical state analyses supported this conclusion (Supplementary Fig. 10).

Interestingly, we observed a polarization response in a 30-nm-thick $H_xK_{1-x}GaSb_2$ nanosheet (one-capacitor system) and in a 30-nm-thick $H_xK_{1-x}GaSb_2$ nanosheet covered with a non-ferroelectric insulator (20-nm-thick HfO_2; two-capacitor system), as measured with piezoresponse force microscopy (PFM; Fig. 2d). Reitveld refinement confirmed that $H_xK_{1-x}GaSb_2$ exhibited the *mmm* centrosymmetric point group (Supplementary Table 9). Second harmonic generation experiments also confirmed the centrosymmetric structure of $H_xK_{1-x}GaSb_2$ (Supplementary Fig. 11). This indicated, in principle, that no ferroelectric or even piezoelectric behaviour would be observed.

However, given that (1) HfO_2 is non-ferroelectric[17] (Supplementary Fig. 12) and (2) ferroelectric-like polarization switching was observed under an external electric field, as shown with the PFM phase (Fig. 2e) and the PFM amplitude (Fig. 2f) versus voltage hysteresis loop, we attributed the observed ferroelectric-like characteristics to charged defect migration on the surface or along the layers under applied electric fields, which is referred to as electrochemical polarization, as seen in $LiCoO_2$ (ref. 18). This polarization was induced by K^+ ion migration via K vacancies. Furthermore, we noticed changes in the coercive voltage with thickness (Fig. 2g–h and Supplementary Fig. 13); the coercive voltage increased with increasing thickness due to the higher electric field required for polarization. Initially, no PFM response was observed for ternary $KGaSb_2$. However, when the K^+ ions were removed, polarization occurred, and then polarization disappeared again when the number of K^+ ions exceeded a critical value (Fig. 2i and Supplementary Fig. 14). This correlation between K^+ ion content and PFM response provided additional evidence for K^+ ion migration.

This scenario was further supported by surface potential (V_{surf}) mapping with Kelvin probe force microscopy on Au-contacted $H_xK_{1-x}GaSb_2$ (Fig. 2j), yielding several key findings. First, the V_{surf} value of $H_xK_{1-x}GaSb_2$ was 0.3 V more negative than that of Au ($q\Phi_{Au}$ = 5.1 eV, where q is charge and Φ_{Au} is the work function potential of Au; ref. 19; Fig. 2k), indicating a higher work function ($q\Phi_{H_xK_{1-x}GaSb_2} \approx 5.4$ eV) and confirming a Schottky barrier at the p-type $H_xK_{1-x}GaSb_2$/Au interface[20]. Conversely, V_{surf} of $H_xK_{1-x}GaSb_2$ was 0.29 V higher than that of Pt, indicating ohmic contact ($q\Phi_{H_xK_{1-x}GaSb_2} < q\Phi_{Pt}$), confirmed by current–voltage (I_D–V_D) curves (I_D, drain current; V_D, drain voltage; Supplementary Fig. 15). Second, applying V_D = 5 V induced observable changes in Kelvin probe force microscopy images, with V_{surf} decreasing on the drain side and increasing on the source side (Fig. 2k), attributed to K^+ ion migration. This change resulted from the migration of K^+ ions from the drain to the source, causing hole accumulation on the drain side and depletion on the source side (Fig. 2l). Third, elemental mapping confirmed reduced K^+ ion concentration on the drain side and increased concentration on the source side (Supplementary Fig. 16), aligning with V_{surf} changes indicating hole accumulation and depletion.

https://doi.org/10.1038/s41563-024-01986-x

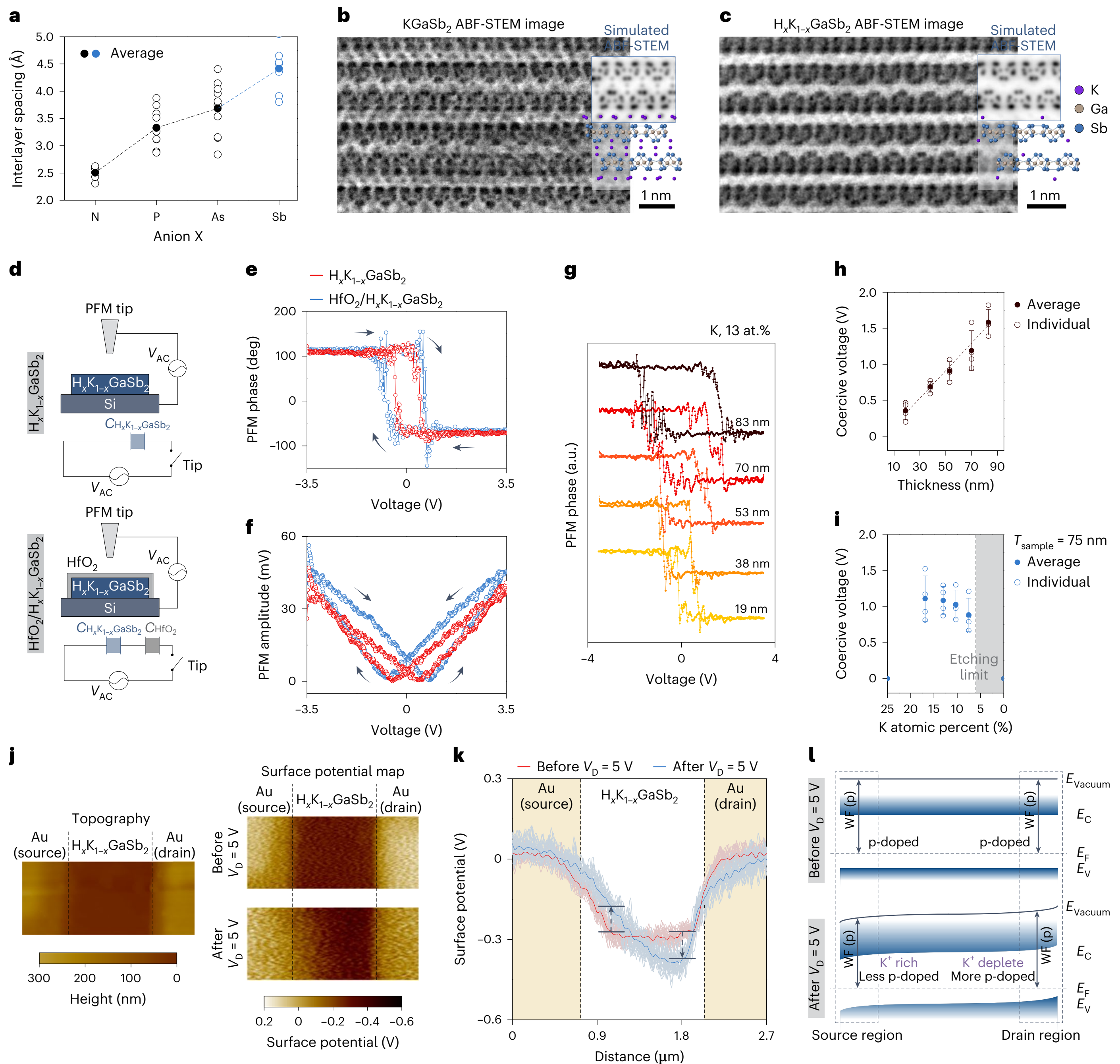

Fig. 2 | The vdW $H_xK_{1-x}GaSb_2$ crystal and electrochemical polarization. **a**, Comparison of the interlayer spacings of cation-eutaxy A_x–B_y–X_z compounds. Each empty and filled circle represents the individual and averaged interlayer spacing of the cation-eutaxy A_x–B_y–X_z compounds for each anion, respectively. **b**,**c**, Annular bright-field (ABF)-STEM images of $KGaSb_2$ (**b**) and $H_xK_{1-x}GaSb_2$ (**c**) with large fields of view, along the [110] zone axis. Simulated ABF-STEM images and atomic configurations for each compound are shown in the insets. **d**, Schematics of the PFM measurements and corresponding equivalent short-circuit diagrams for 30-nm-thick $H_xK_{1-x}GaSb_2$ (one-capacitor ($C_{H_xK_{1-x}GaSb_2}$) system) and 20-nm-thick HfO_2/30-nm-thick $H_xK_{1-x}GaSb_2$ (two-capacitor ($C_{HfO_2}/C_{H_xK_{1-x}GaSb_2}$) system) with AC voltage (V_{AC}). **e**,**f**, PFM phase hysteresis loops (**e**) and amplitude hysteresis loops (**f**) as functions of the voltage sweep (±3.5 V) for 30-nm-thick $H_xK_{1-x}GaSb_2$ (red) and 20-nm-thick HfO_2/30-nm-thick $H_xK_{1-x}GaSb_2$ (blue). **g**, PFM phase hysteresis loops of $H_xK_{1-x}GaSb_2$ (K, 13 at.%) nanosheets depending on the thickness (19, 38, 53, 70 and 83 nm) as a function of the voltage sweep (±3.5 V). **h**, Coercive voltages are plotted against thickness, using empty and filled circles to denote coercive voltage data and averaged coercive voltage, respectively. **i**, The coercive voltages of 75-nm-thick (T_{sample} = 75 nm) $H_xK_{1-x}GaSb_2$ as a function of the K^+ ion proportion (25, 16.9, 13, 10.3, 7.5 and 0 at.%). The empty and filled circles represent the coercive voltage data and the averaged coercive voltage, respectively. The error bars in **h** and **i** represent s.d. from four different devices. **j**, Topography and surface potential (V_{surf}) maps of the Au-contacted $H_xK_{1-x}GaSb_2$ device before and after applying V_D = 5 V. **k,** V_{surf} line profile of the Au-contacted $H_xK_{1-x}GaSb_2$ device based on V_{surf} mapping data. V_{surf} profiles of Au-contacted $H_xK_{1-x}GaSb_2$ device before and after V_D = 5 V are shown: averaged profiles in red and blue, and thirty randomly selected profiles in light red and light blue, respectively. After applying V_D = 5 V, V_{surf} decreased by 0.11 ± 0.03 V on the drain side and increased by 0.1 ± 0.03 V on the source side. **l**, Band alignment of $H_xK_{1-x}GaSb_2$ before (top) and after (bottom) applying V_D = 5 V. WF, E_{Vacuum}, E_C, E_F and E_V indicate work function, global vacuum level, the bottom of the conduction band, Fermi level and the top of the valence band, respectively.

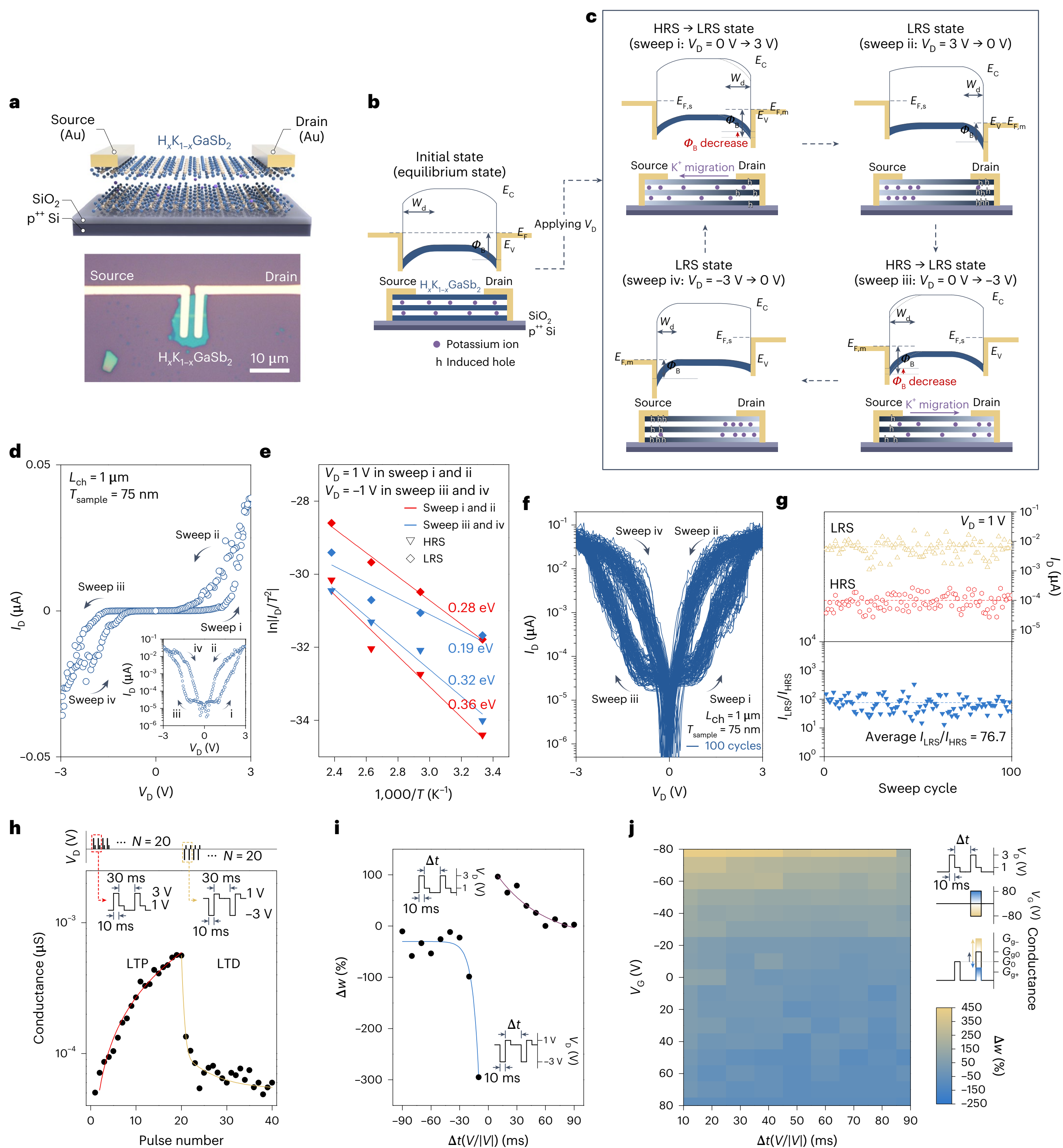

Memristive switching enabled by vdW gap

To investigate the ion-migration-derived electrical properties, we examined memristive switching of a lateral $H_xK_{1-x}GaSb_2$ device (Fig. 3a). In this set-up, we used exfoliated $H_xK_{1-x}GaSb_2$ with Au contacts, which formed a Schottky barrier at the metal–semiconductor interface (Fig. 3b). During a sweep of the positive V_D from 0 V to 3 V (sweep i), the memristive device initially exhibited a high-resistance state (HRS) and gradually transitioned to a low-resistance state (LRS; Fig. 3c). This transition occurred because the Schottky barrier height (Φ_B) at the drain region decreased as holes accumulated at the interface of $H_xK_{1-x}GaSb_2$ and the drain caused by K^+ ion migration to the source. The device maintained the LRS during the sweep from 3 V to 0 V (sweep ii). However, upon crossing zero voltage, it reset from the LRS to the HRS as hole movement from the source to the semiconductor was impeded by Φ_B. Subsequently, during the voltage sweep from 0 V to −3 V, K^+ ions migrated to the drain region, causing Φ_B in the source region to decrease gradually; this resulted in a transition from the HRS to the LRS (sweep iii), which was identical to that of sweep i. The LRS was maintained during the V_D sweep from −3 V to 0 V (sweep iv). The memristive switching based on ion migration was clearly observed in the I_D–V_D plot (Fig. 3d).

Fig. 3 | Memristive characteristics of 4*O*-$H_xK_{1-x}GaSb_2$. **a**, Schematic of the two-terminal device (top) and an image of the fabricated device (bottom). **b**, Band diagram and corresponding cross-sectional schematic of $H_xK_{1-x}GaSb_2$ in the static state. **c**, Band diagrams and corresponding schematics during the full-sweep cycle: HRS → LRS (sweep i; left top); LRS (sweep ii; right top); HRS → LRS (sweep iii; right bottom); and LRS (sweep iv; left bottom). W_d, $E_{F,m}$ and $E_{F,s}$ indicate depletion width, metal Fermi level and semiconductor Fermi level, respectively. **d**, I_D–V_D curve (channel length (L_{ch}) = 1 µm, T_{sample} = 75 nm). The semilogarithmic curve is shown in the inset. **e**, Arrhenius plot extracted from the I_D–V_D plot in the temperature range 300–420 K. The Φ_B values were extracted at V_D = 1 V in sweeps i and ii (red) and at V_D = −1 V in sweeps iii and iv (blue). The Φ_B values of the HRS and LRS are marked with triangles and diamonds, respectively. **f**, 100 full-switching cycles of $H_xK_{1-x}GaSb_2$. **g**, Stability for the HRS and LRS (top) and the I_{LRS}/I_{HRS} (bottom) for 100 sweep cycles. Dash lines represent the averaged I_{LRS}, I_{HRS} (top) and I_{LRS}/I_{HRS} (bottom) for 100 sweep cycles, respectively. **h**, Long-term potentiation (LTP) and long-term depression (LTD) with consecutive stimulation of 20 excitatory and 20 inhibitory spikes (the number of spikes (N) = 20, V_D = ±3 V, spike width (W_{spike}) = 10 ms, Δt = 30 ms). The conductance was measured with a V_{read} (1 V, 10 ms). **i**, Δw as a function of Δt between positive (3 V) and negative (−3 V) paired V_D spikes (W_{spike} = 10 ms). Conductance was measured with a V_{read} (1 V, 10 ms). Δw is defined as the ratio of the difference in conductance between the second and first synaptic spikes to the conductance of the first synaptic spike. **j**, Δw as a function of Δt and V_G spikes. Positive paired V_D spikes were programmed as a function of Δt. V_G spikes were applied only during the second synaptic spikes, and their corresponding conductance was measured. G_0, G_{g0}, G_{g+} and G_{g-} were measured with a V_{read} (1 V, 10 ms), where G_0 is the conductance of the first synaptic spike, and G_{g0}, G_{g+} and G_{g-} are the conductances of the second synaptic spike when V_G is 0 V, positive and negative, respectively.

We next examined hole transport during a V_D sweep to determine if it is influenced by Schottky barrier modulation, using the $\ln|I_D|$ and $|V_D|^{1/4}$ relationship, indicative of thermionic emission over the barrier[21,22]. Supplementary Fig. 17 shows a linear correlation, confirming that the memristive switching in $H_xK_{1-x}GaSb_2$ stems from Schottky barrier modulation rather than filament formation. This conclusion is supported by the absence of memristive behaviour in Pt-contacted $H_xK_{1-x}GaSb_2$ devices (Supplementary Fig. 18). Moreover, I_D–V_D measurements across temperatures (300 K to 420 K; Supplementary Fig. 19) allowed extraction of Φ_B values for the HRS and LRS based on the slope of $\ln|I_D/T^2|$ versus 1,000/T (T, temperature; refs. 23,24), revealing reductions from 0.36 eV to 0.28 eV (HRS to LRS) during sweeps i to ii and from 0.32 eV to 0.19 eV (HRS to LRS) during sweeps iii to iv (Fig. 3e).

Figure 3f illustrates the endurance characteristics, subjected to 100 full-sweep cycles between the LRS and HRS. The K^+ ions used the vdW gap as an ion migration pathway, which was expected to possess a low activation energy and enable stable operation without requiring an electroforming process. Full switching occurred at low V_D values of ±3 V, more than 20 times lower than when using grain boundaries as the defect migration paths[25], suggesting the potential for low-power operation. Figure 3g shows the HRS and LRS currents (I_{HRS} and I_{LRS}, respectively) at V_D = 1 V and the corresponding switching ratio (I_{LRS}/I_{HRS}) over 100 cycles. The I_{LRS}/I_{HRS} ratio can also be adjusted by varying the thickness of $H_xK_{1-x}GaSb_2$ (Supplementary Fig. 20).

Similar memristive behaviour and electrochemical polarization were observed for other materials, including 1*Q*-$H_{2x}Ca_{1-x}GaN$, *2M*-$H_xNa_{2-x}Ga_2As_3$, *3R*-$H_{2x}Ca_{1-x}Ga_2As_2$, 2*M*-$H_xNa_{2-x}Al_2Sb_3$, *2H*-$H_{2x}Ca_{1-x}In_2P_2$, *2M*-$H_xK_{2-x}In_2As_3$ and *2M*-$H_xK_{2-x}In_2Sb_3$, as well as unknown compounds such as $H_xK_{2-x}In_2P_3$ and $H_xNa_{2-x}In_2As_3$, all of which featured the remaining cation A (Supplementary Fig. 21).

The two-terminal $H_xK_{1-x}GaSb_2$ device mimicked synaptic functions in neuromorphic systems, with channel conductance representing synaptic weight controlled by consecutive spikes at the drain terminal[26,27]. Through 20 consecutive positive (3 V) and negative (−3 V) V_D spikes, postsynaptic conductance changed exponentially, emulating synaptic potentiation and depression behaviours (Fig. 3h). We also mimicked indirect spike-timing-dependent plasticity by adjusting temporal intervals (Δt) between positive/negative paired V_D spikes (Fig. 3i). Pairing positive/negative V_D spikes with shorter (longer) Δt induced a greater (lesser) positive/negative synaptic weight change (Δw). The Δw exhibited a negative exponential relationship with Δt, similar to the biological update rule[28].

Furthermore, we investigated the emulation of heterosynaptic plasticity with a three-terminal $H_xK_{1-x}GaSb_2$ memtransistor. By applying a gate voltage (V_G), we modulated the conductance of $H_xK_{1-x}GaSb_2$ (Supplementary Fig. 22), demonstrating that synaptic weight modulation could be extended beyond V_D spikes to V_G spikes at the gate terminal. Initially, Δw was induced by positive paired V_D spikes with Δt. Subsequently, channel conductance modulation was facilitated by V_G spikes coinciding with second synaptic spikes, with conductance recorded. Notably, increasing the V_G spike magnitude to a negative value, coupled with decreasing Δt, resulted in greater Δw (Fig. 3j). Therefore, Δw was influenced by both Δt and V_G spikes. Considering that (1) potentiation/depression was regulated by two variables and (2) a threshold sliding effect was observed (Supplementary Fig. 23), it was evident that a higher-order synaptic function resembling the BCM rule was implemented[28]. This represents an instance of implementing gate-tunable indirect spike-timing-dependent plasticity using a semiconducting memristor.

Programmable logic functions of the memtransistor

We employed $H_xK_{1-x}GaSb_2$ to construct a logic device integrating ion-movement-based memory with the semiconductor functionality of the channel (Fig. 4a). To investigate the gate tunability of the memristive behaviour, we analysed the hysteretic I_D–V_D behaviour with electrostatic gating (Fig. 4b and Supplementary Fig. 24). The V_G was varied from −80 V to 80 V, causing an approximately 50-fold change in both I_{HRS} and I_{LRS}. Nonetheless, the memristive switching behaviour remained consistent, suggesting that V_G influenced the channel conductance rather than the switching mechanism. This was supported by the stable data retention shown in Fig. 4c. Importantly, we observed a threshold voltage (V_{th}) of 30 V for the LRS device, whereas the V_{th} was 12 V for the HRS device; thus, a logic window could be built in a single channel without controlling the gate oxide (Fig. 4d).

To demonstrate the OR logic, we initiated the configuration of the channel to a HRS using a current of V_D = −4 V. Two input lines, I_1 (gate) and I_2 (drain), were introduced (Fig. 4a). Briefly, I_1 controlled channel

Fig. 4 | Logic gates in a single 4*O*-$H_xK_{1-x}GaSb_2$ memtransistor. **a**, Schematic illustration of the $H_xK_{1-x}GaSb_2$ memtransistor. The back gate and the drain electrode serve as inputs 1 (I_1) and 2 (I_2), respectively. **b**, Semilogarithmic I_D–V_D curve at V_G (from −80 V to 80 V). **c**, The data retention in the HRS (beige), HRS with V_G = −40 V (blue), LRS (red) and LRS with V_G = −40 V (black) measured at V_D = 1 V. **d**, Transfer curves of the $H_xK_{1-x}GaSb_2$ memtransistor in different resistance states measured, exhibiting a shift in V_{th} from V_{th} = 12 V in the HRS (blue) to V_{th} = 30 V in the LRS (black). **e**, Individual band diagrams for different inputs. For I_1 = 0, V_G = 0 V; for I_1 = 1, V_G = −40 V; for I_2 = 0, V_D = 0 V prior to V_{read}; and for I_2 = 1, V_D = 4 V prior to V_{read}. I_1 was applied simultaneously with V_{read}, whereas I_2 was applied before V_{read} to induce a change in the resistance state. **f**, Sequential four input states (top), OR logic gate (bottom) and corresponding truth table (bottom right). Each state is indicated as follows: A, HRS at V_G = 0 V; B, HRS at V_G = −40 V; C, LRS at V_G = 0 V; and D, LRS at V_G = −40 V. **g**, Individual band diagrams for different inputs after reprogramming. For I_1 = 0, V_G = 0 V; for I_1 = 1, V_G = 40 V; for I_2 = 0, V_D = 0 V prior to V_{read}; and for I_2 = 1, V_D = −4 V prior to V_{read}. The logic input (I_1, I_2) performance is indicated by letters: A, I_1I_2 = 00; B, I_1I_2 = 10; C, I_1I_2 = 01; and D, I_1I_2 = 11. **h**, Four input states (top), NOR logic gate (bottom) and corresponding truth table (bottom right). Each state is indicated as follows: A, LRS at V_G = 0 V; B, LRS at V_G = −40 V; C, HRS at V_G = 0 V; and D, HRS at V_G = −40 V.

conductance via gate tunability, whereas I_2 toggled the resistance within the channel between the HRS and LRS (Fig. 4e). For I_1, $V_G = 0$ V represents logic state 0, while −40 V represents logic state 1. For I_2, logic state 0 was set with $V_D = 0$ V prior to read voltage (V_{read}) at 1 V, and logic state 1 was set with $V_D = 4$ V prior to V_{read}. Subsequently, we characterized the OR logic by measuring the output related to I_1 and I_2.

Figure 4f presents representative input/output data for the input combination I_1I_2 (00 → 10 → 01 → 11). The outputs for different I_1I_2 input combinations revealed that the output current levels for logic states 0 and 1 were distinctly different: logic state 0 for an I_1I_2 input of 00 (labelled as A), logic state 1 for an I_1I_2 input of 01 (labelled as B), logic state 1 for an I_1I_2 input of 10 (labelled as C) and logic state 1 for an I_1I_2

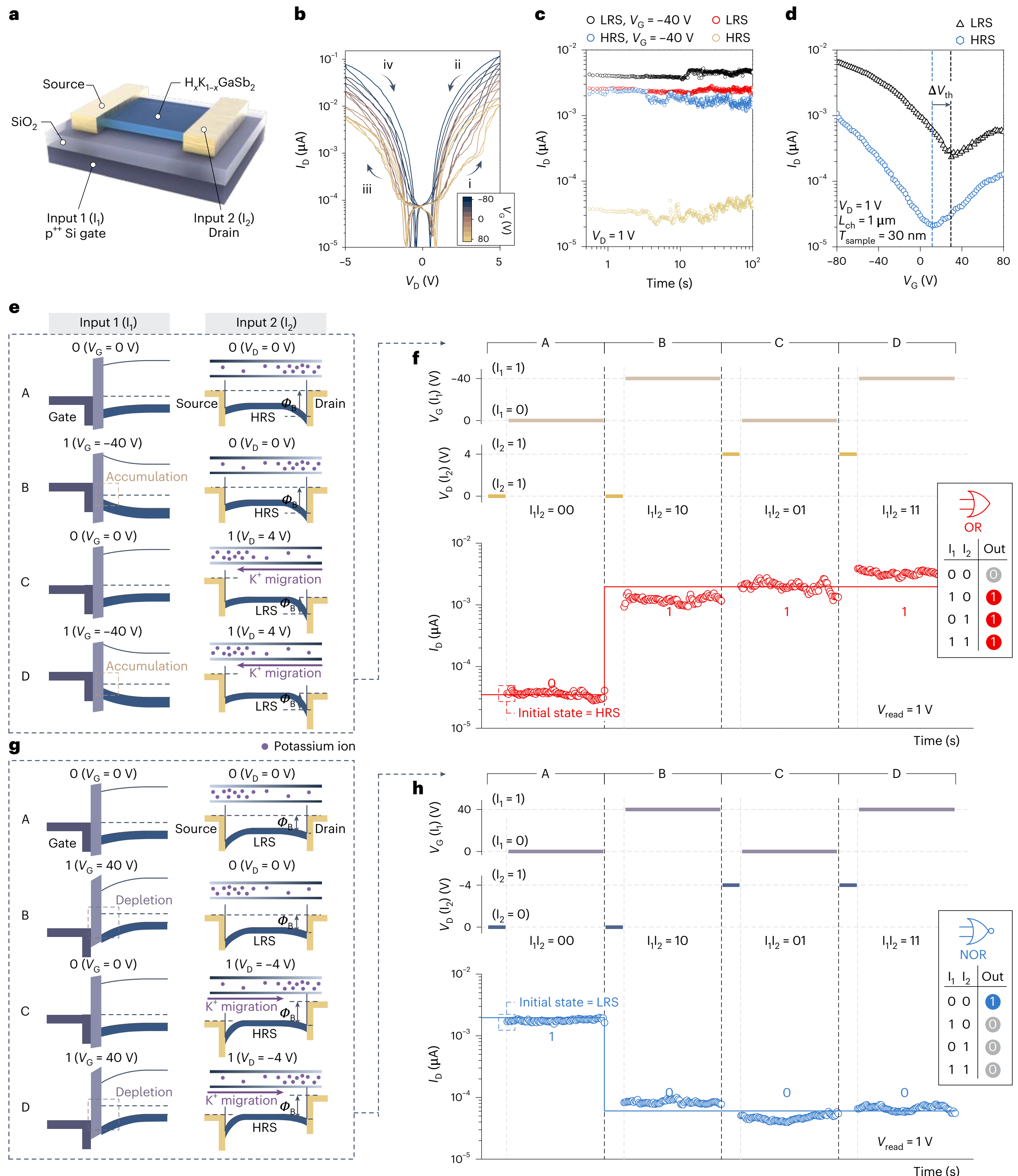

input of 11 (labelled as D). These output values, summarized in a truth table, illustrated the current distribution for both logic states 0 and 1.

Notably, the same single device exhibited versatility in performing various distinct logic operations owing to its reprogrammable resistance state (Fig. 4g). To underscore this essential feature, we reprogrammed the same device to attain a LRS (by applying $V_D = 4$ V) for operation as a NOR logic device. For I_1, an input voltage of 0 V represented logic state 0, and 40 V represented logic state 1. For I_2, an input voltage of 0 V prior to V_{read} signified a logic state of 0, while −4 V prior to V_{read} denoted logic state 1. Subsequent tests revealed that the output for four typical input combinations (Fig. 4h) exhibited distinctly different output ranges for logic states 1 and 0 at $V_{read} = 1$ V. These results have been summarized in a truth table for the NOR logic. Logic operations could be optimized by adjusting the gate voltage (I_1), channel resistance (I_2) and V_{th}. In contrast to traditional methods that use a ferroelectric dielectric alongside a semiconductor channel for logic functions[29], our approach integrates both memory and logic functions within the channel. Importantly, we expanded the material options to include III–V compounds, addressing the limited availability of ferroelectric semiconductors[30].

Discussion

We have presented experimental realization of synthesizing a diverse family of protonated III–V vdW crystals, exhibiting semiconducting and ferroelectric-like electrochemical polarization properties. By electrostatically gating semiconducting III–V materials and using cation migration, using the vdW gap for the cation migration pathway, we created multiple electrical states within the channel, enhancing functionality and control in transistor operation. Consequently, we demonstrated the synaptic function and the implementation of logic functions in a single-gate memtransistor, even without ferroelectric dielectrics or additional node selection. Challenges remain, including defining descriptors for cation-eutaxy structures, achieving exfoliation to monolayers and scaling up synthesis for practical applications. Nonetheless, the introduction of the III–V vdW crystal presents an addition to the realm of 2D pnictides, potentially enriching the landscape already occupied by the well-explored 2D transition metal dichalcogenides from group VI (ref. 31) and halide perovskites from group VII (ref. 32). The understanding gained from using our method will enable future synthetic efforts and allow for new types of vdW crystals that can be used in the fields of electronics, photonics and catalysis and potentially many other fields.

Online content

Any methods, additional references, Nature Portfolio reporting summaries, source data, extended data, supplementary information, acknowledgements, peer review information; details of author contributions and competing interests; and statements of data and code availability are available at https://doi.org/10.1038/s41563-024-01986-x.

References

1. Xiao, X., Wang, H., Urbankowski, P. & Gogotsi, Y. Topochemical synthesis of 2D materials. *Chem. Soc. Rev.* **47**, 8744–8765 (2018).
2. Uppuluri, R., Gupta, A. S., Rosas, A. S. & Mallouk, T. E. Soft chemistry of ion-exchangeable layered metal oxides. *Chem. Soc. Rev.* **47**, 2401–2430 (2018).
3. Xia, Q. & Yang, J. J. Memristive crossbar arrays for brain-inspired computing. *Nat. Mater.* **18**, 309–323 (2019).
4. Yan, X., Qian, J. H., Sangwan, V. K. & Hersam, M. C. Progress and challenges for memtransistors in neuromorphic circuits and systems. *Adv. Mater.* **34**, 2108025 (2022).
5. Chen, S. et al. Wafer-scale integration of two-dimensional materials in high-density memristive crossbar arrays for artificial neural networks. *Nat. Electron.* **3**, 638–645 (2020).
6. Pi, S. et al. Memristor crossbar arrays with 6-nm half-pitch and 2-nm critical dimension. *Nat. Nanotechnol.* **14**, 35–39 (2019).
7. Li, M. et al. Imperfection-enabled memristive switching in van der Waals materials. *Nat. Electron.* **6**, 491–505 (2023).
8. Geselbracht, M. J., Richardson, T. J. & Stacy, A. M. Superconductivity in the layered compound Li_xNbO_2. *Nature* **345**, 324–326 (1990).
9. Peng, J. et al. Stoichiometric two-dimensional non-van der Waals $AgCrS_2$ with superionic behaviour at room temperature. *Nat. Chem.* **13**, 1235–1240 (2021).
10. Hantanasirisakul, K. & Gogotsi, Y. Electronic and optical properties of 2D transition metal carbides and nitrides (MXenes). *Adv. Mater.* **30**, 1804779 (2018).
11. Belsky, A., Hellenbrandt, M., Karen, V. L. & Luksch, P. New developments in the Inorganic Crystal Structure Database (ICSD): accessibility in support of materials research and design. *Acta Crystallogr. B Struct. Sci.* **58**, 364–369 (2002).
12. Jain, A. et al. Commentary: the Materials Project: a materials genome approach to accelerating materials innovation. *APL Mater.* **1**, 011002 (2013).
13. Ong, S. P. et al. Python Materials Genomics (pymatgen): a robust, open-source python library for materials analysis. *Comput. Mater. Sci.* **68**, 314–319 (2013).
14. Hautier, G., Fischer, C., Ehrlacher, V., Jain, A. & Ceder, G. Data mined ionic substitutions for the discovery of new compounds. *Inorg. Chem.* **50**, 656–663 (2011).
15. Rohrer, G. S. *Structure and Bonding in Crystalline Materials* (Cambridege Univ. Press, 2001).
16. Kang, K., Meng, Y. S., Bréger, J., Grey, C. P. & Ceder, G. Electrodes with high power and high capacity for rechargeable lithium batteries. *Science* **311**, 977–980 (2006).
17. Schroeder, U., Park, M. H., Mikolajick, T. & Hwang, C. S. The fundamentals and applications of ferroelectric HfO_2. *Nat. Rev. Mater.* **7**, 653–669 (2022).
18. Balke, N. et al. Nanoscale mapping of ion diffusion in a lithium-ion battery cathode. *Nat. Nanotechnol.* **5**, 749–754 (2010).
19. Lide, D. R. (ed.) *CRC Handbook of Chemistry and Physics* 77th edn (CRC Press, 1996).
20. Streetman, B. G. *Solid State Electronic Devices* 3rd edn (Prentice Hall, 1990).
21. Liu, K. et al. An optoelectronic synapse based on α-In_2Se_3 with controllable temporal dynamics for multimode and multiscale reservoir computing. *Nat. Electron.* **5**, 761–773 (2022).
22. Xue, F. et al. Gate-tunable and multidirection-switchable memristive phenomena in a van der Waals ferroelectric. *Adv. Mater.* **31**, 1901300 (2019).
23. Kwon, G. et al. Interaction- and defect-free van der Waals contacts between metals and two-dimensional semiconductors. *Nat. Electron.* **5**, 241–247 (2022).
24. Bessonov, A. A. et al. Layered memristive and memcapacitive switches for printable electronics. *Nat. Mater.* **14**, 199–204 (2015).
25. Sangwan, V. K. et al. Multi-terminal memtransistors from polycrystalline monolayer molybdenum disulfide. *Nature* **554**, 500–504 (2018).
26. Zhu, X., Li, D., Liang, X. & Lu, W. D. Ionic modulation and ionic coupling effects in MoS_2 devices for neuromorphic computing. *Nat. Mater.* **18**, 141–148 (2019).
27. Li, Y. et al. Anomalous resistive switching in memristors based on two-dimensional palladium diselenide using heterophase grain boundaries. *Nat. Electron.* **4**, 348–356 (2021).
28. Gerstner, W., Kistler, W. M., Naud, R. & Paninski, L. *Neuronal Dynamics: from Single Neurons to Networks and Models of Cognition* (Cambridge Univ. Press, 2014).

29. Khan, A. I., Keshavarzi, A. & Datta, S. The future of ferroelectric field-effect transistor technology. *Nat. Electron.* **3**, 588–597 (2020).
30. Si, M. et al. A ferroelectric semiconductor field-effect transistor. *Nat. Electron.* **2**, 580–586 (2019).
31. Bae, J. et al. Kinetic 2D crystals via topochemical approach. *Adv. Mater.* **33**, 2006043 (2021).
32. Mao, L., Stoumpos, C. C. & Kanatzidis, M. G. Two-dimensional hybrid halide perovskites: principles and promises. *J. Am. Chem. Soc.* **141**, 1171–1190 (2019).
33. Pauling, L. The principles determining the structure of complex ionic crystals. *J. Am. Chem. Soc.* **51**, 1010–1026 (1929).

Publisher's note Springer Nature remains neutral with regard to jurisdictional claims in published maps and institutional affiliations.

Springer Nature or its licensor (e.g. a society or other partner) holds exclusive rights to this article under a publishing agreement with the author(s) or other rightsholder(s); author self-archiving of the accepted manuscript version of this article is solely governed by the terms of such publishing agreement and applicable law.

© The Author(s), under exclusive licence to Springer Nature Limited 2024

Jihong Bae[1,2,17], Jongbum Won[1,2,17], Taeyoung Kim[1,2], Sangjin Choi[1,2], Hyesoo Kim[1,2], Seung-Hyun Victor Oh[1], Giyeok Lee[1], Eunsil Lee[1,2,3], Sijin Jeon[1,2,3], Minjung Kim[1,2], Hyung Wan Do[1,2], Dongchul Seo[1,2,4,5], Sungsoon Kim[1,2], Youngjun Cho[1,2], Hyeonsoo Kang[1,2], Bokyeong Kim[1,2], Hong Choi[1,2], Jihoon Han[1,2], Taehoon Kim[1,2], Narguess Nemati[6], Chanho Park[1], Kyuho Lee[1], Hongjae Moon[1], Jeongmin Kim[7], Hyunggeun Lee[8], Daniel W. Davies[9], Dohyun Kim[8], Seunghun Kang[10], Byung-Kyu Yu[4,5], Jaegyeom Kim[3], Min Kyung Cho[11], Jee-Hwan Bae[11], Soohyung Park[11], Jungkil Kim[12], Ha-Jun Sung[8], Myung-Chul Jung[8], In Chung[13], Heonjin Choi[1], Hyunyong Choi[14], Dohun Kim[14], Hionsuck Baik[15], Jae-Hyun Lee[4,5], Heejun Yang[8], Yunseok Kim[10], Hong-Gyu Park[14], Wooyoung Lee[1], Kee Joo Chang[8], Miso Kim[10], Dong Won Chun[11], Myung Joon Han[8], Aron Walsh[1,9], Aloysius Soon[1] ✉, Jinwoo Cheon[4,5,16] ✉, Cheolmin Park[1] ✉, Jong-Young Kim[3] ✉ & Wooyoung Shim[1,2,4,5] ✉

[1]Department of Materials Science and Engineering, Yonsei University, Seoul, Korea. [2]Center for Multi-Dimensional Materials, Yonsei University, Seoul, Korea. [3]Icheon Branch, Korea Institute of Ceramic Engineering and Technology, Icheon, Korea. [4]Center for Nanomedicine, Institute for Basic Science (IBS), Seoul, Korea. [5]Graduate Program of Nano Biomedical Engineering (NanoBME), Advanced Science Institute, Yonsei University, Seoul, Korea. [6]Department of Mechanical and Production Engineering, Aarhus University, Aarhus, Denmark. [7]Division of Nanotechnology, DGIST, Daegu, South Korea. [8]Department of Physics, Korea Advanced Institute of Science and Technology, Daejeon, Korea. [9]Thomas Young Centre and Department of Materials, Imperial College London, London, UK. [10]School of Advanced Materials and Engineering, Sungkyunkwan University, Suwon, Korea. [11]Advanced Analysis Center, Korea Institute of Science and Technology, Seoul, Korea. [12]Department of Physics, Jeju National University, Jeju, Korea. [13]School of Chemical and Biological Engineering, and Institute of Chemical Process, Seoul National University, Seoul, Korea. [14]Department of Physics and Astronomy, and Institute of Applied Physics, Seoul National University, Seoul, Korea. [15]Korea Basic Science Institute Seoul, Seoul, Korea. [16]Department of Chemistry, Yonsei University, Seoul, Korea. [17]These authors contributed equally: Jihong Bae, Jongbum Won. ✉e-mail: aloysius.soon@yonsei.ac.kr; jcheon@yonsei.ac.kr; cmpark@yonsei.ac.kr; jykim@kicet.re.kr; wshim@yonsei.ac.kr

https://doi.org/10.1038/s41563-024-01986-x

Methods

Classification of cation-eutaxy compounds

Cation-eutaxy compounds are classified based on four distinct features encompassing the elemental combinations and bonding characteristics of the interlayer and intralayer structures. These features are essential for the selective removal of cation A from A_x–B_y–X_z ternary compounds via soft chemistry methods. The classification criteria are as follows. (1) Ionicity of A–X bond: cation A must exhibit a stronger ionic character in the A–X bond than in the B–X bond. This requires cation A to have lower electronegativity than cation B, enabling the formation of an ionic bond with X rather than a polar covalent bond between B–X. (2) Two-dimensional polyhedron connectivity: the intralayer polyhedra of B–X are interconnected in a manner analogous to 2D crystals. This connectivity involves primary bonding between B–X and polyanionic bonding. The resulting [BX] framework exhibits a layered morphology resembling a sheet rather than a one-dimensional rod-like structure. (3) Distinct cation planes: cations A and B are not situated in the same plane, indicating a departure from simple compositional ordering. The [BX] layer is sandwiched between the layers consisting solely of cation A to create a distinct arrangement. (4) Absence of interlayer primary bonding: no primary bonding exists between the polyhedra of B–X along the *z* axis, signifying the absence of interlayer X–X and BX–BX bonds along the stacking direction. By considering these four features, we could effectively classify cation-eutaxy compounds and identify their unique structural characteristics.

Data-driven crystal structure prediction and DFT evaluation for identifying unknown compounds

An ionic substitution algorithm was used to predict accessible cation-eutaxy A_x–B_y–X_z crystal structures; this algorithm used a statistical model pretrained on a comprehensive database of known compounds, including oxidation state information. When used predictively, a combination of species of interest (elements in given oxidation states) was substituted onto lattice sites in structures from the dataset of known materials. Each species substitution was associated with a certain probability, which came from the trained model. If the overall probability for a given set of substitutions was above a certain threshold, it was added to a list of possible structures. For each of the 3,510 chemical compositions of interest, this procedure was carried out by using the pool of 972 eutaxy-motif compounds, and the probability was calculated. We considered common oxidation states for the A and B elements, as defined within pymatgen, and allowed for mixed valency of the X element when X is in group V, as this was required for a subset of the compounds. We used a probability threshold of 1×10^{-8}, which was the smallest threshold that still returned all of the experimentally realized eutaxy compounds in this work. We used a revised version of the model that was trained using pnictide compounds and was implemented in pymatgen (ref. 34). Applying an ion substitution algorithm to 760 known compounds enabled the identification of potential unknown compounds with reasonable probability scores, yielding 1,827 suggested compounds. Among these, 575 candidates exhibiting the highest probabilities within each A–B–X combination were chosen for subsequent evaluation based on formation energies. Of these candidates, 127 'unknown' compounds displayed energy levels above the convex hull (E_{hull}) with a difference of less than 0.2 eV per atom, suggesting their potential synthesizability. While compounds with an E_{hull} > 0.2 eV per atom may still be viable for synthesis, we chose to adopt a threshold of 0.2 eV per atom for metastability in our high-throughput screening approach. This choice was made to enhance the reliability of identifying unknown cation-eutaxy candidates. By establishing a threshold, we aimed to prioritize the most promising candidates with a higher likelihood of stability and experimental feasibility.

Total interaction energies (U) of ternary compounds

To find candidates for cation-eutaxy III–V-based ternary compounds, we performed electrostatic interaction energy calculations for A_x–B_y–X_z ternary compounds featured in the Materials Project database with a given oxidation number and stoichiometry. The total interaction energy (U) can be written as $U = |(Z_A \times Z_B)/d_{AB}| + |(Z_B \times Z_X)/d_{BX}| - |(Z_A \times Z_X)/d_{AX}|$, where cation A is an alkali metal (group I) or alkaline earth metal (group II), cation B is a group III element and anion X is a group V element. We used the valence (Z) of each ion to calculate the total interaction energy (U) with Robocrystallographer (ref. 35; v.0.1.3) in Materials Project. When electrostatic neutrality in the compound can be explained by only one valence (Z), the mixed oxidation states were considered, and the number of valence electrons was averaged and assigned equally to all ion sites. To obtain reasonable structures in terms of thermodynamic stability, the E_{hull} for all ternary compounds was limited to 0.1 eV per atom. As the U value increased, we identified a tendency for compounds to possess cation-eutaxy structures, which was clearly observed when ternary compounds were classified based on their crystal structure (Bravais lattice). Because of the absence of cation-eutaxy prototypes, we excluded ternary compounds with triclinic and cubic structures from the list of cation-eutaxy candidates. Finally, we acquired 35 candidates for cation-eutaxy ternary compounds from 1,415 A-III–V compounds in the Materials Project database.

$KGaSb_2$ and $H_xK_{1-x}GaSb_2$ syntheses

First, 0.4 g of K trace metal (1.02 mmol, Sigma-Aldrich, 99% purity), 0.72 g of Ga trace metal (1.03 mmol, Sigma-Aldrich, 99.999% purity) and 1.88 g of Sb beads (1.54 mmol, Sigma-Aldrich, 99.999% purity) were used to synthesize $KGaSb_2$. Then, 3 g of this mixture with a 1:1:2 ratio of K/Ga/Sb was placed in an alumina crucible and loaded into a quartz double ampoule inside a glove box under an inert Ar atmosphere. The quartz double ampoule was extracted from the glove box and flame-sealed to avoid oxidation of the sample due to potassium-induced corrosion of the quartz. To obtain large single crystals, a box furnace was used to provide appropriate control of the growth process. First, the double ampoule was heated to 750 °C at a rate of 250 °C h^{-1} and maintained at that temperature for 40 h to fully dissolve and mix the K, Ga and Sb. Then, the double ampoule was slowly cooled from 750 °C to 500 °C over a period of 100 h and maintained at 500 °C for 100 h to grow $KGaSb_2$ crystals. Then, the double ampoule was cooled to room temperature at a rate of 100 °C h^{-1}. Finally, the synthesized crystals were mechanically separated from the crucible in the glove box. Plate-like silver $KGaSb_2$ crystals with lateral sizes of 2–3 mm were obtained. An etchant was prepared prior to the synthesis of $H_xK_{1-x}GaSb_2$. Gallium chloride (Thermo Fisher Scientific, 99.999% purity) was left in the atmosphere to absorb moisture and form an aqueous solution. The $KGaSb_2$ powder precursor (0.05 g) was placed in the aqueous gallium chloride and warmed at 50 °C for 6 h. Afterward, ethylene glycol (99.8%, anhydrous, Sigma-Aldrich) was used to remove the potassium chloride salt. Then, methanol was used to wash out the ethylene glycol. Black $H_xK_{1-x}GaSb_2$ powder was obtained by drying under vacuum for 24 h.

High-resolution electron microscopy and STEM image simulation

The atomic structures of $KGaSb_2$ and $H_xK_{1-x}GaSb_2$ were characterized with STEM (JEOL JEM-ARM200F) with a spherical aberration corrector. HAADF and annular bright-field images were collected simultaneously. The system was operated at an accelerating voltage of 200 kV and equipped with silicon drift detector (SDD) (with an active area of 100 mm^2 and a solid angle of 0.9 sr), allowing energy dispersive X-ray spectroscopy (EDS) analyses. Simulated STEM images were obtained with the Dr. Probe program. Simulated STEM images were collected at 300 kV with an aberration-corrected electron probe with an angle of 25 mrad and using the multislice algorithm. The collection angles for the simulated HAADF images were 45–200 mrad. The final geometrical

width of the electron source was accounted for by convolving the simulated image with a Gaussian point spread.

Measurements of ion-migration-derived ferroelectric-like properties

To verify the ferroelectric-like properties, we prepared three samples: (1) HfO_2, (2) $H_xK_{1-x}GaSb_2$ and (3) HfO_2-covered $H_xK_{1-x}GaSb_2$. A patterned p-doped Si substrate was washed with acetone and isopropyl alcohol to remove any residue. To prepare (1) and (2), $H_xK_{1-x}GaSb_2$ nanosheets were exfoliated mechanically on a p-doped Si substrate in an argon-filled glove box. All samples were immersed in acetone for 15 min to eliminate any residue. Then, a 20-nm-thick layer of HfO_2 as a dielectric was grown on samples (1) and (3) via atomic layer deposition at 180 °C. Finally, polarization switching of the three samples was observed with PFM (multimode scanning probe microscope (SPM); Bruker).

Memtransistor device fabrication

The synthesized $H_xK_{1-x}GaSb_2$ nanosheets were mechanically exfoliated with scotch tape from bulk crystals on a 300 nm insulating SiO_2/p-doped Si substrate in an argon-filled glove box. The substrate with the prepared nanosheet on top was immersed in acetone for 30 min to eliminate the residue. After the photoresist polymethyl methacrylate was spin-coated onto the sample, the source and drain terminals were patterned by electron-beam lithography. Then, thermal evaporation and sputtering were performed to deposit 80-nm-thick Au. We chose Au for the contact metal because Au has a relatively low work function compared to that of $H_xK_{1-x}GaSb_2$, resulting in the formation of a Schottky barrier. The p-doped Si was used as the bottom gate. Lift-off was subsequently conducted in warm acetone. Electrical measurements were performed with a Keithley 4200A semiconductor characterization system at room temperature and in an ambient environment.

Data availability

The data that support the other findings of this study are available from the corresponding authors upon reasonable request. Source data are provided with this paper. Other relevant information in this study is included in the Supplementary Information.

References

34. Sun, W. et al. Thermodynamic routes to novel metastable nitrogen-rich nitrides. *Chem. Mater.* **29**, 6936–6946 (2017).
35. Ganose, A. M. & Jain, A. Robocrystallographer: automated crystal structure text descriptions and analysis. *MRS Commun.* **9**, 874–881 (2019).

Acknowledgements

This work was supported by the National Research Foundation (NRF) of Korea through a grant funded by the Korean government (2018M3D1A1058793) and a grant from the Institute for Basic Science (IBS-R026-D1). We are grateful to the UK Materials and Molecular Modelling Hub for providing computational resources, which were partially funded by the Engineering and Physical Sciences Research Council (EPSRC; EP/T022213/1).

Author contributions

J.B., J.W., Taeyoung Kim, S.C., Hyesoo Kim, J.C., Cheolmin Park, J.-Y.K. and W.S. designed the experiments. J.B., J.W., Taeyoung Kim, S.C., Hyesoo Kim, E.L., S.J., Minjung Kim, S. Kim, Y.C., B.K., Hong Choi and J.H. synthesized the materials. J.B., Minjung Kim, H.W.D., D.S., H. Kang, Taehoon Kim, N.N., H.M., Jeongmin Kim, Dohyun Kim, W.L. and Heonjin Choi developed the devices and performed the measurements. S.-H.V.O., G.L., H.L., H.-J.S., M.-C.J., K.J.C., M.J.H. and A.S. performed the first-principles calculations and analyses, while D.W.D. and A.W. developed the data-driven models. Chanho Park, K.L., S. Kang, Jungkil Kim, I.C., Hyunyong Choi, Dohun Kim, H.Y., Y.K., H.-G.P., Miso Kim and Cheolmin Park analysed the characteristics. J.B., J.W., S.C., H. Kim, E.L., B.-K.Y., Jaegyeom Kim, M.K.C., J.-H.B., S.P., H.B., J.-H.L., D.W.C., J.-Y.K. and W.S. performed the structural analysis. All authors wrote the manuscript and contributed to the overall scientific interpretation.

Competing interests

The authors declare no competing interests.

Additional information

Supplementary information The online version contains supplementary material available at https://doi.org/10.1038/s41563-024-01986-x.

Correspondence and requests for materials should be addressed to Aloysius Soon, Jinwoo Cheon, Cheolmin Park, Jong-Young Kim or Wooyoung Shim.

Peer review information *Nature Materials* thanks Gerbrand Ceder and the other, anonymous, reviewer(s) for their contribution to the peer review of this work.

Reprints and permissions information is available at www.nature.com/reprints.